A Robust Nonlinear Model Predictive Controller for a Post-Combustion CO_2 Capture Absorber Unit

Gabriel D. Patron[a], Luis Ricardez-Sandoval[a]*

[a] Department of Chemical Engineering, University of Waterloo, Waterloo, ON, Canada N2L 3G1

Abstract

This study presents the design of a robust nonlinear model predictive controller (NMPC) for the absorber unit of a post-combustion CO_2 capture process operating downstream from a coal-fired power plant. The controller employs a dynamic mechanistic model for this process, which allows for a precise treatment of the sources of uncertainty. In the case of the absorber, the model enables explicit consideration of uncertainty in the process operating conditions dictated by upstream units and in physical property parameters associated with phenomenological descriptions of the process. Using the multi-scenario approach, discrete realizations of the uncertain parameters inside a given uncertainty region can be incorporated into the controller to produce control actions that result in a robust operation in closed-loop. The multi-scenario controller was tested under several disturbance rejection scenarios of varying complexity and their performance was assessed against that of single-scenario NMPCs. The benefits of the robust NMPC approach were most evident for longer simulations and, considering the continuous nature of a power plant and its emissions, make the robust NMPC approach suitable for the operation of this process in the presence of uncertainty and disturbances.

Keywords: Post-combustion CO_2 capture; Process Uncertainty; Model Predictive Control

*Corresponding author: e-mail: laricard@uwaterloo.ca, phone: (+1)519 888 4567 x38667, fax, (+1) 519 888 4347

1. Introduction

As global economic growth continues, an ever-increasing industrial demand bolsters worldwide greenhouse gas (GHG) emissions. CO_2 is the most abundant of the GHGs, totaling 73% of all emissions in 2017, mainly because of its production in the power generation and transportation sectors [1]. In particular, combustion sources make up 89% of the total CO_2 emissions subdivided by fuel type into coal (40%), oil (21%), and natural gas (18%) [1]. After a brief plateau in 2015 and 2016, CO_2 emissions continued their upward trend in 2017 owing to the increasing reliance of developing countries on coal as a convenient energy source [2]. Despite recent trends of waning coal use in in the developed world, worldwide reliance on other CO_2 emitters has been steadily increasing [3]; likely because of their abundance and low price. While it would be ideal to eliminate these emissions, this is not a realistic option because of the worldwide dependency on CO_2 emitting products, thereby necessitating the development of technologies to mitigate global CO_2 emissions.

Carbon capture and storage (CCS) has garnered attention over the last few decades as it aims to reduce the amount of CO_2 released from industrial sources. In particular, pre-combustion removal [4,5], post-combustion removal [6], chemical looping combustion (CLC) [7,8], and oxy-combustion [9,10] have received much attention.

Post-combustion CSS (PCC) is the most mature CCS technology that is ready for deployment. A major benefit of the technology is that it can be used to retrofit existing CO_2 emission sources for immediate removal. For PCC, several methods of removing CO_2 from combustion products in industrial flue gases have been investigated, these include adsorption, physical absorption, chemical absorption, cryogenic separation, and membrane-based separation [11]. Of these, chemical absorption by way of amine solvents has seen experimental contributions by way of pilot-scale [12,13] and industrial-scale [14,15] plants. Moreover, there have also been computational contributions in modelling, simulation and process design [16-22].

Of the solvents possible for chemical absorption PCC, monoethanolamine (MEA) based solvents have received particular attention among the solvent alternatives because of their abundance, performance, and low price relative to other solvents [23]. Consequently, MEA-based chemical absorption for CO_2 removal is very developed as a potential emerging technology since its chemistry and process have been extensively studied [24-28]. Importantly, these studies have allowed the development of transient mechanistic process models [29-31].

For real-life deployment of the MEA-based PCC, the process operation must be well understood to achieve safety and productivity. A crucial part of the operation is the implementation of a process control system to ensure set-point regulation and tracking. In an MEA-based PCC plant, the control system is conventionally used to ensure that CO_2 removal targets and energy consumption requirements are met in the presence of upstream disturbances, e.g. changes in the energy load. The successful fulfillment of these operational goals is especially pertinent in the PCC system as the CO_2 removal generally detracts from the profitability of the upstream plant. In addition to the control studies that consider conventional decentralized feedback controllers such as PI and PID [32,33], the development of the aforementioned PCC plant models has enabled the use of model-based control strategies. Previous studies have implemented model-based control featuring various levels of model sophistication and control envelopes. For the MEA-based PCC plant, Bedelbayev, Greer and Lie [34] implemented an MPC based on a linearized model of the absorber unit whereas Sahraei and Ricardez-Sandoval [35] developed an MPC involving multiple inputs and outputs

and compared their performance to a decentralized feedback PI-based control strategy. He, Sahraei and Ricardez-Sandoval [36] implemented another linearized MPC model integrated with scheduling for the full MEA-based PCC plant. Moreover, Panahi and Skogestad [37] evaluated different control structures for the PCC plant and implemented a multivariable linear MPC. For increasingly complex models, Åkesson et al. [38] considered a low-order nonlinear model and implemented a nonlinear MPC (NMPC) for the absorber unit in the PCC plant. Decardi-Nelson, Liu and Liu [39] also implemented an NMPC scheme for the complete post-combustion MEA-based CCS pilot-scale plant. Additionally, they also developed an economic MPC (EMPC) for the plant. Similarly, Chan and Chen [40] also implemented an EMPC scheme based on an Aspen Plus model of an entire MEA-based CSS plant whereby the process economics can be optimized and controlled with respect to changing feed qualities and utility prices. These are only selected few of the control studies for the MEA-based PCC plant, a review on this subject can be found elsewhere [41].

A complicating factor embedded in the models that are used in model-based control approaches, including those using highly detailed nonlinear mechanistic models, is that the models will be subject to various types of uncertainty. These are caused by assumptions made in developing the model (structural), and error associated with estimating experimental parameters (parametric) [42]. This uncertainty, which leads to mismatch between the plant and the model, can be either exogenous or endogenous. Exogenous uncertainty occurs due to factors not embedded in the model, e.g. variations in inlet compositions, flowrates, changes in products demands; while endogenous uncertainties occur within the model's parameters or equations leading to plant-model mismatch, e.g. activity coefficients, heat transfer coefficients, rate constants. For model-based control, taking these uncertainties into account is crucial as neglecting them will lead to poor controller performance; which would translate into off-specification products, failure to meet commercial and regulatory process demands, and lost profits. To take these uncertainties into account, the closed-loop operation must be made insensitive to uncertainty, which can be achieved through stochastic or robust methods control, the latter of which will the focus of this study. A review of stochastic MPC methods can be found elsewhere [43]. In this context, control actions must be determined such that the process will exhibit good performance in closed-loop despite these uncertainties. The robust operation of the MEA-based PCC has been addressed using optimal control by a few authors. For instance, Panahi and Skogestad [37] employed a robust linear MPC on the entire plant; while Zhang, Turton and Bhattacharyya [44] implemented a H_∞ robust controller with a nonlinear NAARX model on the entire plant. Decardi-Nelson, Liu and Liu [39] evaluated the performance of their NMPC and EMPC schemes under upstream uncertainties; however, they did not make their controllers robust to those uncertainties.

One optimization approach that has not been considered to make the MEA-based PCC plant robust through its control is the multi-scenario approach. In general, scenario-based approaches are commonly used when considering robust operation using MPC under uncertainty whereby an optimal controller considers multiple discrete realizations of uncertainty and aims to find optimal control actions that can accommodate all the pre-specified uncertainty realizations. The multi-scenario approach, as implemented in the present work, has previously been used for a large-scale nonlinear model of an air separation unit [45], and linear hydrodynamic model for water resource management [46]. To the authors' knowledge, the past robust controllers applied to the MEA PCC plant have used linear and reduced-order models while this study uses a nonlinear dynamic mechanistic model for this process. Such a model

enables the controller to explicitly address uncertainty where it is most likely to occur; in parameters associated to specific chemical phenomena and in the process operating conditions dictated by upstream units.

The aim of this study is to use a mechanistic dynamic model to implement and assess the performance of a robust NMPC on the absorber in an MEA-based PCC pilot-scale plant. To the authors' knowledge, this is the first study that has implemented robust control in the MEA-based PCC process (or any other CCS process) with the multi-scenario approach while using the actual mechanistic model of the process. This work explicitly accounts for exogenous uncertainty that will affect the absorber daily owing to changes in operating policies of the upstream emission-producing plant (e.g. rapid changes in flue gas flowrates and uncertainty in flue gas composition); as well as endogenous parametric uncertainty in the plant model via its thermodynamic properties.

This paper is organized as follows: Section 2 outlines the mechanistic MEA-based PCC absorber model in detail. Section 3 revises the formulation for NMPC and extends that formulation for a multi-scenario NMPC. Section 4 gives detail regarding the model implementation and validation whereas Section 5 presents the results of various robust control tests on a simulated MEA-based absorber. Finally, concluding remarks and future work are discussed in Section 6.

2. MEA Absorber model

The dynamic mechanistic model used in this work was adapted from Harun et al. [29] and describes an MEA-based CO_2 absorber unit in a PCC pilot plant as a packed column. The arrangement and operating conditions are based on the pilot plant studied by Dugas [12]. The model is a partial differential algebraic system of equations (PDAEs) as it is composed of ordinary (ODEs) and partial differential equations (PDEs) as well as algebraic equations (AEs).

The absorber, shown in Figure 1, operates at atmospheric inlet pressure and has four components: monoethanolamine (MEA), carbon dioxide (CO_2), water (H_2O), and nitrogen gas (N_2), which are denoted as the set $i = \{MEA, CO_2, H_2O, N_2\}$. The column has two inlet and two outlet streams located at the bottom and the top of the column's axial domain ($z(m)$), which are at $z = 0$ and $z = H$, respectively. The top inlet stream, referred to as the "lean" amine stream, consists of a liquid phase mixture of MEA, CO_2, and H_2O. In the full PCC plant, this stream comes from a storage tank that mixes fresh MEA with the recycled MEA from a downstream stripper that regenerates and recycles the solvent. The bottom inlet of the column, referred to as the flue gas stream, consists of CO_2, H_2O, and N_2. This gaseous mixture comes from an upstream combustion source and contains the CO_2 for removal. The top outlet stream, referred to as the vent gas, consists of unremoved CO_2 as well as H_2O and N_2. The bottom outlet stream, referred to as the "rich" amine stream consists of all four components and goes to the aforementioned stripper for isolation of the CO_2 and regeneration of the amine solvent. Inside the column, a small amount of gaseous CO_2 is naturally absorbed into the liquid phase from the gas phase. More importantly, the absorption relies on the reactive mechanism that takes advantage of the weak acid and base properties of the CO_2 and MEA (or other alkanolamines), respectively. These two components react to make a water-soluble salt containing the CO_2, which readily dissolves into the liquid phase rich amine solution. A detailed description of this mechanism can be found in [47].

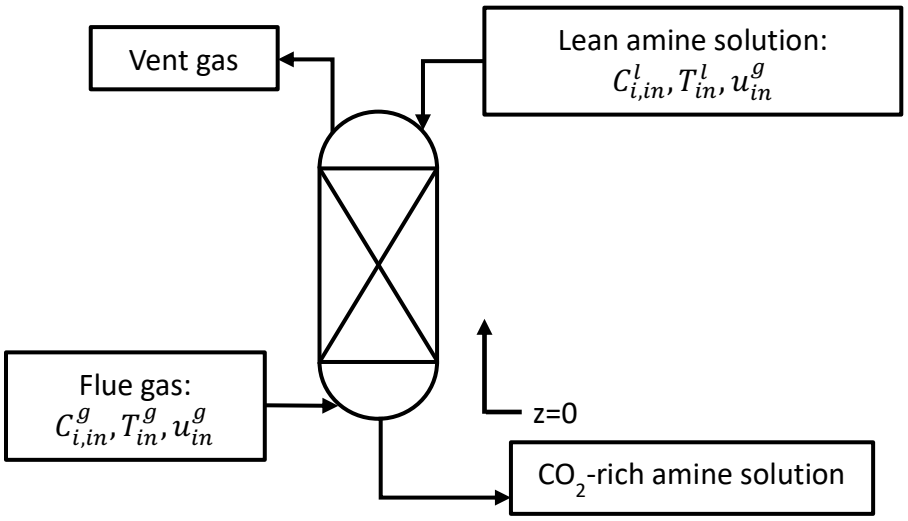

Figure 1: Absorber column arrangement with inputs and outputs. Components are MEA, CO2, H2O, and N2

The absorber model considered in this study operates under the following assumptions:

1. There is turbulent flow within the column, which is approximated as plug flow.
2. The system is modelled as axially distributed and is assumed to be well-mixed in the radial direction.
3. The gas phase is ideal owing to low operating pressures.
4. The pressure drop along the height of the column is linear.
5. N_2 only exists in the gas phase, phase changes occur in all other components in both directions.
6. There is thermal equilibrium between the phases.
7. There is no accumulation in gas and liquid films.
8. The liquid phase has a constant velocity in the axial domain for a given inlet flowrate.

This model consists of molar component balances for the gas and liquid phases, energy balances for the gas and liquid phases, rate equations, chemical kinetic equations, equilibrium equations, and physical property descriptions. These are presented next.

2.1. Molar component material balance

The molar component material balances describe the dynamics of the constituent component concentration in each phase owing to chemical reactions, changes in equilibria, and mass transfer. They are as follows:

$$\frac{dC_i^l}{dt} = u_l \frac{\partial C_i^l}{\partial z} + a_w N_i \tag{1}$$

$$\frac{dC_i^g}{dt} = -u_g \frac{\partial C_i^g}{\partial z} - a_w N_i - C_i^g \frac{\partial u_g}{\partial z} \tag{2}$$

where $C_i^l(mol/m^3)$ and $C_i^g(mol/m^3)$ are liquid and gas molar concentrations of component i, respectively; and $u_l(m/s)$ and $u_g(m/s)$ are liquid and gas velocities, respectively. $a_w(m^2/m^3)$ is the wetted area, while $N_i(mol/m^2/s)$ is the molar flux between phases for component i. The molar flux directions are defined as positive for gains of material in the liquid phase and, accordingly, negative for gains of material in the gas phase.

While the assumptions stated that there is a fixed liquid velocity along the height of the column for a given liquid inlet flowrate, the same is not assumed for the gas velocity since the gas phase is much less dense and loses substantially more momentum as it travels up the column. This decrease in velocity is expressed as a momentum balance for the gas phase:

$$\frac{\partial u_g}{\partial z} = \frac{u_g}{P}\frac{dP}{dz} + \frac{u_g}{T_g}\frac{dT_g}{dz} - \frac{a_w}{C_{tot}^g}\sum_{i=1}^{4} N_i \tag{3}$$

where $P(bar)$ is the absorber pressure as a function of position in the axial domain, $T_g(K)$ is the gas phase temperature, and $C_{tot}^g = \sum_{i=1}^{4} C_i^g \ (mol/m^3)$ is the total gas concentration.

2.2. Energy balance

The energy balances describe the dynamics of the temperatures of the two phases owing to chemical reactions, equilibria, and heat transfer. They are stated as follows:

$$\frac{dT_l}{dt} = u_l\frac{\partial T_l}{\partial z} - \frac{a_w}{\sum_{i=1}^{4} c_{p,i}^l\, C_i^l}\left[h_{gl}\left(T_l - T_g\right) + \Delta H_{rxn} N_{CO_2} - \Delta H_{H_2O}^{vap} N_{H_2O} + h_{out}(T_l - T_{amb})\right] \tag{4}$$

$$\frac{dT_g}{dt} = -u_g\frac{\partial T_g}{\partial z} + \frac{a_w}{\sum_{i=1}^{4} c_{p,i}^g\, C_i^g}\left[h_{gl}\left(T_l - T_g\right)\right] \tag{5}$$

where $T_l(K)$ is the liquid phase temperature, $h_{gl}(J/mol/K)$ is the interfacial heat transfer coefficient given by the Chilton-Colburn heat and mass transfer analogy [48], and $T_{amb}(K)$ is the temperature of the surroundings. $c_{p,i}^l(J/mol/K)$ and $c_{p,i}^g(J/mol/K)$ are the liquid and gas specific heat capacities of component i, respectively; N_{CO_2} and N_{H_2O} are the molar fluxes of CO_2 and H_2O, respectively, calculated using the two-film mass transfer model. $\Delta H_{rxn}(J/mol)$ is the molar heat of reaction, $\Delta H_{H_2O}^{vap}(J/mol)$ is the molar heat of vaporization of water, and h_{out} ($W/m^2/K$) is the heat transfer coefficient between the absorber and its surroundings.

2.3. Mass Transfer

The two-film model gives the rate of mass transfer within the absorber for all components excluding N_2, as it is assumed to only occur in the gas phase. The model is stated as follows:

$$N_i = K_i^g(p_i - p_i^*) \tag{6}$$

$$\frac{1}{K_i^g} = \frac{1}{k_i^g} + \frac{He_i}{k_i^l E_{abs}} \tag{7}$$

where $K_i^g(mol/m^2/Pa/s)$ is the overall mass transfer coefficient for the gas phase while $k_i^g(mol/m^2/Pa/s)$ and $k_i^l(m/s)$ are the binary gas and liquid mass transfer coefficients for component i, respectively. $p_i(kPa)$ and $p_i^*(kPa)$ are the partial and equilibrium pressures for component i, respectively. $He_i(kPa\ m^3/mol)$ is the Henry's law constant for component i. The use of an overall mass transfer coefficient eliminates the need to calculate interfacial concentrations and, as stated earlier, transfer from the gas to the liquid phase was used as the convention for positive mass transfer. The model assumes that resistance to mass transfer for liquid H_2O and MEA is negligible because these components have a higher solubility; thus, most of their resistance to mass transfer occurs in the gas phase [29].

As mentioned above, the acid-base chemical reactions between CO_2 and MEA described by Austgen et al. [49] dictates the amount of CO_2 absorbed in the liquid phase solvent. The effect of this increase is captured by the enhancement factor (E_{abs}), which represents an approximate analytical solution to the differential equations governing the diffusional mass transfer and chemical reactions occurring in the liquid film. The enhancement factor is valid under the pseudo-first order reaction scheme with respect to CO_2; which is valid in the situation where an alkanolamine is absorbing CO_2 in a packed column, owing to the increased mixing afforded by the packing [27]. This scheme is facilitated by low CO_2 partial pressure, high reactant concentration, and short contact times; thus, ensuring that mass transfer is enhanced by the reactions while not depleting the amine concentration. The volume of amine is considered constant throughout the film and equal to that of the bulk phase. The enhancement factor is given by:

$$E_{abs} = \frac{\sqrt{k_2 C^*_{MEA} D_{CO_2}}}{k^l_{CO_2}} \tag{8}$$

where $k_2(m^2/mol/s)$ is the second-order reaction rate constant and $C^*_{MEA}(mol/m^3)$ is the liquid molar concentration of free MEA, both calculated from Hoff et al. [26]. $D_{CO_2}(m^2/s)$ is the diffusivity of CO_2 in the MEA solution.

2.4. Equilibria

The dynamic model considers chemical and phase equilibria together. Chemical equilibrium describes the balance between ionic and molecular species in the liquid phase while phase equilibrium describes the balance between phases at the gas-liquid interface. For H_2O and MEA, the equilibrium pressure at the interface is expressed as follows:

$$p^*_i = x_i \gamma_i p^{vap}_i \tag{9}$$

where x_i, γ_i, and $p^{vap}_i(kPa)$ are the liquid fraction, activity coefficient, and vapor pressure of component i, respectively. Since the temperature of the system exceeds the supercritical temperature of CO_2, it does not exist in the liquid phase. Instead, the equilibrium pressure of CO_2 is calculated using Henry's law:

$$p^*_{CO_2} = He_{CO_2} C^*_{CO_2} \gamma_{CO_2} \tag{10}$$

where $C^*_{CO_2}(mol/m^3)$ is the liquid molar concentration of free CO_2 from Hoff et al. [26], and γ_{CO_2} is the activity coefficient of CO_2.

2.5. Physical Properties, Absorber Design, and Model Inputs

Table 1 lists the physical properties used in the model, their sources, and values (if constant). Variable physical properties are calculated using correlations provided in the corresponding reference. Table 1 also lists the packed column design characteristics as used in this study. Additionally, Table 2 lists the required inputs for the model, which come in the form of initial conditions and inlet (boundary) operating conditions. Initial conditions are obtained from measurements/estimates from the absorber while operating conditions are obtained from measurements/estimated from upstream units.

Table 1: Physical properties and design characteristics used for the absorber column model

Physical Property	**Value**	**Source**
Ambient Temperature (K)	$T_{amb} = 297.6$	Harun et al. [29]

Heat transfer coefficient between absorber and surroundings (W/m2/K)	$h_{out} = 430$	Kvamsdal and Rochelle [50]
Molar heat of reaction (kJ/mol)	$\Delta H_{rxn} = 48$	Kvamsdal and Rochelle [50]
Molar heat of vaporization (kJ/mol)	$\Delta H_{H_2O}^{vap} = 82$	Poling, Prausnitz and O'Connell [51]
MEA activity coefficient	$\gamma_{MEA} = 0.677$	Aspen Property Package
CO_2 activity coefficient	$\gamma_{CO_2} = 0.381$	Smith, Van Ness and Abbott [52]
H_2O activity coefficient	$\gamma_{H_2O} = 0.974$	Smith, Van Ness and Abbott [52]
Wetted area (m^2/m^3)	a_w	Onda, Takeuchi and Okumoto [28]
Liquid component heat capacity ($J/mol/K$)	$c_{p,i}^l$	Hilliard [53]
Gas component heat capacity ($J/mol/K$)	$c_{p,i}^g$	Aspen Property Package
Liquid component mass transfer coefficient (m/s)	k_i^l	Onda, Takeuchi and Okumoto [28]
Gas component mass transfer coefficient ($mol/m^2/Pa/s$)	k_i^g	Onda, Takeuchi and Okumoto [28]
Component Henry's law constant ($kPa\ m^3/mol$)	He_i	Haimour and Sandall [24]
Second-order reaction rate constant ($m^2/mol/s$)	k_2	Hikita et al. [25]
CO_2 diffusivity in solvent solution (mol/m^3)	D_{CO_2}	Ko et al. [54]
Component vapour pressure (bar)	p_i^{vap}	Aspen Property Package
Design Characteristics		
Column internal diameter (m)	0.43	Cerrillo-Briones and Ricardez-Sandoval [55]
Packing height (m)	6.1	Cerrillo-Briones and Ricardez-Sandoval [55]
Packing type	IMTP #40	Cerrillo-Briones and Ricardez-Sandoval [55]

Table 2: Model inputs: initial and operating conditions required

	Initial Condition $(\mathbf{0} \leq \boldsymbol{z} \leq \boldsymbol{H}, \boldsymbol{t} = \mathbf{0})$	***Boundary Condition*** $(\boldsymbol{z} = \mathbf{0}, \boldsymbol{z} = \boldsymbol{H}, \boldsymbol{t} \geq \mathbf{0})$
Gas	$C_i^g(z,0) = C_{i,o}^g(z)$	$C_i^g(0,t) = C_{i,in}^g(t)$
	$T^g(z,0) = T_o^g(z)$	$T^g(0,t) = T_{in}^g(t)$
		$u^g(0,t) = u_{in}^g(t)$
		$P^g(0,t) = P_{in}^g(t)$
Liquid	$C_i^l(z,0) = C_{i,o}^l(z)$	$C_i^l(H,t) = C_{i,in}^l(t)$
	$T^l(z,0) = T_o^l(z)$	$T^l(H,t) = T_{in}^l(t)$
		$u^l(z,t) = u_{in}^l(t)$

The outlined PDEs that comprise the mass and energy balances (Equations 1-5) are denoted as $\boldsymbol{f}$, while the AEs that comprise the process phenomena (Equations 6-10) and physical property (Table 1) models are denoted as $\boldsymbol{h}$. This set of equations represent the mechanistic model for this process, which require the column design specifications and initial/boundary conditions presented in Tables 1 and 2, respectively.

3. Robust NMPC

In the present work, a nominal NMPC formulation will be implemented along with the multi-scenario formulation for comparison. By nominal NMPC, we refer to an NMPC controller that includes no measures for dealing with uncertainty in the formulation (it assumes that its parameters are known *a priori*). We begin by defining the multi-scenario NMPC and subsequently presenting the nominal NMPC as a special case. Generally, an NMPC uses a nonlinear dynamic process model to determine optimal control actions that minimize a loss function, e.g. set-point tracking errors in the controlled variables. In the case of the multi-scenario NMPC, the controller considers multiple realizations of the model's uncertain parameters, which results in instances of the process model denoted by the set "r". The operation of the NMPC in the feedback control strategy is depicted in Figure 2, which shows a control structure operating at a time t in the operation of a process where an NMPC receives measurements or estimates of the plant states $\boldsymbol{x_0}$ as initial conditions for the model, as well as the set points for the controlled variables $\boldsymbol{y_{t+i}^{sp}}$. This information is included in the formulation of the optimal control problem. For a multi-scenario discrete-time NMPC at sampling time t, this problem is as follows:

$$
\begin{aligned}
&\min_{u_{t+j}\forall j\in\{1,\dots,t+C\}} \sum_{r=1}^{M} \omega_r \left(\boldsymbol{Q} \sum_{i=t}^{P} \left(\widehat{\boldsymbol{y}}_{t+i,r} - \boldsymbol{y}_{t+i,r}^{sp}\right)^2 \right) + \boldsymbol{R} \sum_{j=t}^{C} \Delta \boldsymbol{u}_{t+j}{}^2 \\
&s.t. \\
&\boldsymbol{f}\left(\boldsymbol{x}_{t,r}, \boldsymbol{u}_{t+j}; \boldsymbol{\theta}_r\right) = \widehat{\boldsymbol{x}}_{t+i,r}, \quad \forall i \in \{1,\dots,t+P\}, \quad \forall j \in \{1,\dots,t+C\}, \quad \forall r \in \{1,\dots,M\} \\
&\boldsymbol{x_t} = \boldsymbol{x_0} \\
&\boldsymbol{h}\left(\widehat{\boldsymbol{x}}_{t+i,r}, \boldsymbol{u}_{t+j}; \boldsymbol{\theta}_r\right) = \widehat{\boldsymbol{Y}}_{t+i,r}, \quad \forall i \in \{1,\dots,t+P\}, \quad \forall j \in \{1,\dots,t+C\}, \quad \forall r \in \{1,\dots,M\} \\
&\boldsymbol{g}\left(\widehat{\boldsymbol{x}}_{t+i,r}, \boldsymbol{u}_{t+j}; \boldsymbol{\theta}_r\right) \leq \boldsymbol{0}, \\
&\boldsymbol{u^l} \leq \boldsymbol{u}_{t+j} \leq \boldsymbol{u^h}, \quad \forall j \in \{1,\dots,t+C\}
\end{aligned}
\tag{11}
$$

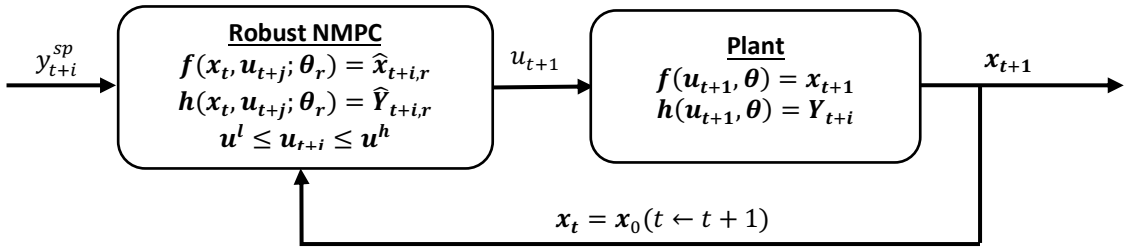

Figure 2: Feedback loop between the simulated plant and multi-scenario NMPC

where $\widehat{\boldsymbol{x}}_{t+i,r} \in \mathbb{R}^{N_x}$ represents the predicted states (differential variables) for each model realization, $\widehat{\boldsymbol{y}}_{t+i,r} \in \mathbb{R}^{N_y}$ are the predicted controlled variables for each model realization, $\boldsymbol{\theta_r} \in \mathbb{R}^{N_\theta}$ are the set of realizations for the uncertain model parameters, and $\widehat{\boldsymbol{Y}}_{t+i,r} \in \mathbb{R}^{N_Y}$ is the vector of predicted outputs (algebraic variables) for each realizations such that $\widehat{\boldsymbol{Y}}_{t+i,r} \supset \widehat{\boldsymbol{y}}_{t+i,r}$**.** Note that these variables are defined as across the set "r", representing the various model realizations corresponding to each realization in the uncertain parameters. $\boldsymbol{y_{t+i}^{sp}} \in \mathbb{R}^{N_y}$ are the user-defined set points for the controlled variables, and $\boldsymbol{x_t} \in \mathbb{R}^{N_x}$ are the measured or estimated states used as the initial condition. Note that these variables are not indexed across the set "r" as they are externally acquired thus realization independent (they have the same value for all realizations). $\boldsymbol{x_0} \in \mathbb{R}^{N_x}$ is the state vector acquired from the simulated plant, which is set as equal to $\boldsymbol{x_t}$ for every NMPC execution thereby enabling feedback to the controller. $\Delta \boldsymbol{u_{t+i}} \in \mathbb{R}^{N_u}$ is the vector of changes in the manipulated variables ($\Delta \boldsymbol{u_{t+i}} = \boldsymbol{u_{t+i}} - \boldsymbol{u_{t+i-1}}$). The controller tuning parameters include diagonal

positive semidefinite matrices $\boldsymbol{Q} \in \mathbb{R}^{N_y \times N_y}$ and $\boldsymbol{R} \in \mathbb{R}^{N_u \times N_u}$, which affect set-point tracking and control move suppression, respectively. P and C, which denote the prediction and control horizons as integer multiples of the sampling intervals, respectively, also serve as tuning parameters as they can affect the controller's performance. $\sum_{r=1}^{M} \omega_r = 1$ are nonnegative weights for different uncertainty realizations where M is the user-defined number of realizations that the NMPC considers. These weights are useful for providing less conservative control actions in the robust NMPC approach if a probability distribution for the realizations is available. As mentioned above, these realizations represent instances of the process model that the NMPC simultaneously considers such that each realization has a unique combination of uncertain parameters. Of the total model parameters, only a user-defined subset is considered uncertain, this subset is chosen based on *a priori* process and model knowledge about which parameters are difficult to estimate**.**

By solving the open-loop problem (11), an optimal control sequence $\boldsymbol{u_{t+1}}, \ldots, \boldsymbol{u_{t+C}}$ is obtained for the user-defined control horizon C. The optimization problem from which this optimal sequence is acquired is subject to the system of constraints composed of the aforementioned DAE system $\boldsymbol{f}$, $\boldsymbol{h}$, and $\boldsymbol{g}$, as well as input constraints $\boldsymbol{u^l} \leq \boldsymbol{u_{t+i}} \leq \boldsymbol{u^h}$. $\boldsymbol{f}: \mathbb{R}^{N_x} \times \mathbb{R}^{N_u} \times \mathbb{R}^{N_\theta} \rightarrow \mathbb{R}^{N_x}$ denotes the set of nonlinear differential equations describing the evolution of states in the system, $\boldsymbol{h}: \mathbb{R}^{N_x} \times \mathbb{R}^{N_u} \times \mathbb{R}^{N_\theta} \rightarrow \mathbb{R}^{N_Y}$ denotes the set of algebraic equations describing the relationships between the states and the outputs of the process models, and $\boldsymbol{g}: \mathbb{R}^{N_x} \times \mathbb{R}^{N_u} \times \mathbb{R}^{N_\theta} \rightarrow \mathbb{R}^{N_Y}$ denotes the set of inequality constraints imposed on the controller (aside from the manipulated variable contraints). $\boldsymbol{u^l}$ and $\boldsymbol{u^h} \in \mathbb{R}^{N_u}$ denote the lower and upper bounds for the manipulated variables and reflect the physical limitations of the process and its controllers. For the multi-scenario NMPC the DAE system composed of $\boldsymbol{f}$, $\boldsymbol{h}$, and $\boldsymbol{g}$ contains "r" realizations of the uncertain parameters $\boldsymbol{\theta_r}$. This DAE system is used to predict the process' evolution for a user specified prediction horizon P for the given uncertainty realizations. This enables the objective function to determine the optimal control actions for the given control horizon. As shown in problem (11), the objective (loss) function contains two weighted terms: one minimizes quadratic deviation from specified set-points and the other penalizes changes in the control actions. From the optimal control sequence obtained by solving problem (11), the first control action $\boldsymbol{u_{t+1}}$ is passed to the plant as depicted in Figure 2. The plant is then simulated for a fixed interval Δt using the input $\boldsymbol{u_{t+1}}$ and a nonlinear process model. This simulation enables the plant states to evolve to $\boldsymbol{x_{t+1}}$ and, after the time interval Δt has elapsed, the process of obtaining and giving measurements/estimates to the NMPC is repeated. By using the evolved states $\boldsymbol{x_{t+1}}$ as feedback to solve problem (11) again recursively during each time interval Δt , the scheme becomes closed-loop. This is shown in the feedback portion of Figure 2 where the initial condition is updated as $\boldsymbol{x_t} = \boldsymbol{x}_0$ after moving the horizon from t to $t + 1$. In this study, we assume full state and disturbance information availability (i.e. the relevant information needed by the NMPC can be precisely measured or estimated). State estimation for the MEA PCC system remains an open challenge that will be addressed in future work. Note that past NMPC studies on this system [38-40] have made similar assumptions. Also note that feedback does not necessarily need to occur at every sampling interval; however, more frequent feedback often leads to better control performance.

The mechanism by which the multi-scenario NMPC makes the controller robust is by finding a single optimal control sequence $\boldsymbol{u_{t+1}}, \ldots, \boldsymbol{u_{t+C}}$ that minimizes the objective function for all model realizations given the feedback $\boldsymbol{x_t} = \boldsymbol{x_0}$ from the plant. This unique optimal control sequence accommodates for the user-defined set of possible values that

uncertainties parameters may manifest during operation. This makes the control actions robust to uncertainty in the sense that although the "true" parameter values are not ascertained by the NMPC controller, the actions will be well-suited for performance across the defined set of uncertain parameter realizations.

As mentioned above, the nominal NMPC occurs as a special case of the multi-scenario NMPC when only a single scenario is considered with no further safeguards against uncertainty. The single scenario corresponds to a nominal realization of the model uncertain parameters, i.e. $\boldsymbol{\theta_r}$, $\forall r \in \{1\}$. This assumption simplifies the formulation and shrinks the model size as variables are no longer indexed across "r", however; it ignores model uncertainty by making the assumption that the model provides a perfect representation of the system. Unfortunately, this often not the case in practice and may result in non-optimal operation because of poor controller performance. Worse still, this assumption may lead to infeasibility.

Both the nominal and multi-scenario NMPC controllers are implemented in a control loop with plant simulation containing a single realization of the uncertain parameters $\boldsymbol{\theta}$. The nominal and multi-scenario NMPC use the large-scale mechanistic model of the absorber column, consisting of $\boldsymbol{f}$ and $\boldsymbol{h}$, presented in Section 2.

4. Model Implementation and validation

The nominal and multi-scenario NMPC optimization formulations are NLP and were implemented in the Pyomo environment, an optimization library in PYTHON [56]. The axially distributed, continuous-time differential-algebraic system presented in Section 2 was discretized axially into ten finite elements using the backward finite difference method. This discretization was determined in the model validation stage by considering different numbers of finite elements for the axial domain. Since there is a tradeoff when considering discretization resolutions between model size and accuracy, a course axial discretization was used to prevent the model from becoming untenably large when discretized in time. The axially discretized absorber model has 80 states and 1,781 algebraic variables. Likewise, the model was discretized in time into eight elements to a step size of 12.5 seconds using three-point Radau collocation on finite elements for all experiments. The Radau collocation method was chosen because of its high accuracy and built-in functionality in Pyomo. The high-resolution discretization in time is necessary because fast responses are observed owing to the fact that the model represents a pilot-scale plant and disturbances are considered directly at the system boundaries, it was found that step sizes larger than 12.5 seconds presented difficulties to the solvers when solving the NMPC problem and smaller sizes would have increased the problem size, making it unnecessarily large. The interior-point optimization algorithm (IPOPT) [57] was used to search for local solutions of the nominal and robust optimization problems presented in (11). The studies presented in this Section were performed on an Intel core i7-4770 CPU @ 3.4GHz. The nominal inlet conditions for the pilot-scale absorber model are adopted from Cerrillo-Briones and Ricardez-Sandoval [55] and are presented in Table 3.

Table 3: Base case inlet operating conditions

	Flue Gas Inlet ($z = 0$)	***Lean Solution Inlet ($z = h$)***
$\boldsymbol{T_{in}(K)}$	319.17	314
$\boldsymbol{y_{in}^{MEA}/x_{in}^{MEA}(mol/mol)}$	0	0.1
$\boldsymbol{y_{in}^{CO_2}/x_{in}^{MCO_2}(mol/mol)}$	0.175	0.030
$\boldsymbol{y_{in}^{H_2O}/x_{in}^{H_2O}(mol/mol)}$	0.025	0.870
$\boldsymbol{y_{in}^{N_2}/x_{in}^{N_2}(mol/mol)}$	0.8	0

$u_{in}(m/s)$	0.64	0.00473

In order to start the controller tests at realistic points, the inlet conditions stated above were used to solve a steady-state version of the nominal absorber model. This steady state provided initial conditions for all undisturbed states at which to begin the dynamic plant simulations. Moreover, the NMPC model's performance in the solver is sensitive to how the algebraic variables are initialized in the solver. This is because the optimization problem is large, containing 64,488 nonlinear algebraic equations and 64,497 variables for the nominal (single-scenario) NMPC. Accordingly, prior to starting test scenarios, a feasibility problem is executed and the algebraic variables from this feasibility problem are used to initialize subsequent NMPC solves.

The model was validated at steady state using the base case operating conditions reported by Harun et al. [29]. These validation operating conditions differ from the base case operating conditions used in this study (shown in Table 3) as they have altered reference fluid velocities. The lower fluid velocities used in this study result in lower carbon capture rates than those considered in the Harun et al. [29]; however, the results obtained are nevertheless representative of the MEA PCC plant. The model was validated at steady state in order to compare the outputs to past implementation of the model, the validation outputs are displayed in Table 4. The outlet stream values were compared to Cerrillo-Briones and Ricardez-Sandoval [55] and Harun et al. [29]. The latter of these studies was itself validated using experimental data from an MEA absorption CCS pilot-scale plant from Dugas [12] and found to be in good agreement.

Table 4: Steady-state validation data for the current absorber model using the base case operating conditions from Harun et al. [29]. Model 1: Cerrillo-Briones and Ricardez-Sandoval [55], Model 2: Harun et al. [29].

	Vent gas			***Rich amine solution***		
	Current model	Model 1	Model 2	Current model	Model 1	Model 2
Temperature (K)	314.45	314.78	314.15	330.61	328.04	327.76
Total molar flowrate (mol/s)	3.49	3.53	3.47	32.87	31.68	32.87
Mole Fraction						
MEA	0.0001	0	0	0.0981	0.1044	0.1021
CO_2	0.0088	0.0108	0.0085	0.0555	0.0502	0.0503
H_2O	0.0717	0.0761	0.0651	0.8464	0.8452	0.8475
N_2	0.9193	0.9066	0.9264	0	0	0

As shown in Table 4, the current model implementation with the base case operating conditions from Harun et al. [29] is in very good agreement for all output values with both models against which it was tested. The output values predicted by the present model have a 4.012% difference and 2.43% difference from model 1 [55] and model 2 [29], respectively; and there are no egregiously inaccurate values. This also validates the choice of resolution for the axial discretization mentioned above. Based on these results, the model was deemed fit for use in the study.

5. Results

In the PCC absorber model presented in Section 2, four parameters were considered uncertain. These included the species activity coefficients in the equilibrium pressure relations ($\gamma_{MEA}, \gamma_{CO_2}, \gamma_{H_2O}$) and the CO_2 flue gas inlet fraction ($y_{in}^{CO_2}$). To the authors' knowledge, this is the first study that explicitly considers uncertainty in these parameters for the post-combustion CO_2 absorber unit. The activity coefficients are featured in the equilibria model (Equation 9); an

earlier study [55] established their significant effect on the system's mass transfer rate. The activity coefficients were chosen as uncertain parameters because they typically exhibit variation with changing operating conditions [49]. This potential variation is addressed in the proposed robust NMPC implementation by treating them as uncertain parameters. Meanwhile, the feed fraction is an inlet condition that is likely to be uncertain due to upstream variations in fuel quality (e.g. change in the type of coal) and demands as well as changes in the operating conditions of the fossil-fired power plants. For simplicity, changes in the CO_2 flue gas inlet mole fraction are reflected only in the H_2O gas inlet mole fraction, so they are treated as a single uncertain parameter. This is assumed because any changes in the upstream process will only affect the relative ratio of combustion products in the flue gas (CO_2 and H_2O), while the fraction of the two non-combustible components will be effectively fixed because there is no MEA in the flue gas and N_2 is inert. Table 5 contains the nominal values for the uncertain parameters considered in this study.

Table 5: Uncertain parameters and their nominal values

Uncertain Parameter (θ)	Nominal Value (θ^{nom})
γ_{MEA}	0.677
γ_{CO_2}	0.381
γ_{H_2O}	0.974
$y_{in}^{CO_2}$	0.175

The nominal NMPC and the multi-scenario NMPC definition from (11) were applied to the CO_2 absorber model presented in Section 2. The formulation of the former will be omitted for brevity as the requisite assumptions were presented above; however, we define the optimization problem for the latter and is as follows:

$$\min_{F_{in,t+j}^{l}\forall j\in\{1,\dots,t+C\}} \sum_{r=1}^{M}\omega_r\left(\sum_{i=t}^{P}\left(\widehat{\%CC}_{t+i,r}-\%CC_{t+i}^{sp}\right)^2\right)+\sum_{j=t}^{C}\Delta F_{l,in_{t+i}}{}^2$$

$$s.t.$$

$$\boldsymbol{f}\left(\boldsymbol{x_t}, F_{l,in_{t+j}}; \boldsymbol{\theta_r}\right)=\hat{\boldsymbol{x}}_{\boldsymbol{t+i,r}}, \quad \forall i,j\in\{1,\dots,t+P\}, \quad \forall r\in\{1,\dots,M\} \tag{12}$$

$$\boldsymbol{x_t}=\boldsymbol{x_0}$$

$$\boldsymbol{h}\left(\hat{\boldsymbol{x}}_{\boldsymbol{t+i,r}}, F_{l,in_{t+j}}; \boldsymbol{\theta_r}\right)=\hat{\boldsymbol{Y}}_{\boldsymbol{t+i,r}}, \quad \forall i,j\in\{1,\dots,t+P\}, \quad \forall r\in\{1,\dots,M\}$$

$$F_{l,in}^{l}\leq F_{l,in_{t+j}}\leq F_{l,in}^{u} \quad \forall j\in\{1,\dots,t+C\}$$

where the manipulated variable is the total liquid feed flowrate F_{in}^{l}, with lower and upper bounds at $F_{l,in}^{l}=10\ mol/s$ and $F_{l,in}^{u}=80\ mol/s$, respectively. This input range provides a physically realistic range for the feed rate while allowing for fast control action. Note that the liquid inlet flowrate is typically used in conjunction with the reboiler duty as manipulated variables when considering an entire MEA PCC plant; in this study however, only the former is used however since it directly affects the absorber being studied and is better suited for disturbance rejection and fast control. As shown in Section 2, the states defined in the differential model equations $\boldsymbol{f}$ for which initial conditions $\boldsymbol{x_t}=\boldsymbol{x_0}$ are required are the component phase concentrations and phase temperatures corresponding to equations (1),(2),(4), and (5). Similarly, the algebraic equations defined in $\boldsymbol{h}$ contain equations (3), (6)-(10) along with physical property relations from Table 1. The control and prediction horizon were both set as 100 seconds, which discretized into eight time intervals ($P=C=8$). This was determined based on preliminary uncontrolled step disturbances tests where the most parsimonious discretization that provided an acceptable resolution for observing dynamics was obtained. The

weighting matrices were set as identity matrices of proper dimensions ($\boldsymbol{Q} = I^{N_y \times N_y}$ and $\boldsymbol{R} = I^{N_u \times N_u}$) and, as no underlying distribution of the expected values of the uncertain parameters is available, the realization weighting parameter is assumed to be equal for all realizations ($\omega_1 = \omega_2 = \cdots = \omega_M$); the latter inherently assumes that the uncertain parameter values are uniformly distributed. The controlled output (variable) in the objective function is set as percentage of CO_2 captured from the flue gas, which will have a unique steady state for a given set of initial and operating conditions. This variable is defined as follows:

$$\%CC = \frac{F_{in}^{CO_2} - F_{out}^{CO_2}}{F_{in}^{CO_2}} \times 100\% \tag{13}$$

For the multi-scenario controllers tested, it is expected that there will be increasing loss in performance as the controller considers a larger number of scenarios. This performance deterioration manifests as less aggressive control actions and eventual set-point offsets. This effect can be examined by comparing the performance of a nominal NMPC under no plant-model mismatch (i.e. the case where the controller knows the plant parameters perfectly) to the performance of the multi-scenario NMPCs. Since the nominal NMPC has a perfect model of the plant, which results in off-set free tracking, it provides an upper limit for controller performance. Thus, for a given controller tuning, the performance of the nominal NMPC can be used as a benchmark to compare the performance of controllers that do result in offset (i.e. robust NMPC controllers and NMPC controllers that consider a plant-model mismatch). To quantify the performance degradation of the robust controller, the price of robustness was used, i.e. the percent difference in performance of the robust controller relative to the nominal NMPC controller. It is expected that the price of robustness (PoR) will increase to reflect increasing conservativeness of multi-scenario NMPCs as they consider more uncertainty realizations in their formulation. PoR is defined as follows:

$$PoR = \left| \frac{J_{robust} - J_{Nominal}}{J_{Nominal}} \right| \times 100\% \tag{14}$$

where "J_{robust}" and "$J_{nominal}$" are the performance indices of a given controller. These terms are defined as the sum of squared errors with respect to a CO_2 removal percentage set-point over a time period (T), i.e.

$$J_c = \sum_{i=0}^{T} (\%CC_i - \%CC_i^{SP})^2, \quad \forall c = \{nominal, robust\} \tag{15}$$

Percent offsets from the desired set-point at the final steady state of simulation were also used for assessment of the robust NMPCs tested. Another factor to consider when using multi-scenario controllers is the increase in size of the multi-scenario NMPC optimization problem. The size of the problem increases proportionally to the number of realizations considered by the controller, thereby increasing the CPU time to solve each optimization problem. Accordingly, averaged CPU times for NMPC executions were also recorded to assess performance in a given simulation.

5.1. Scenario A: Effect of size of uncertainty region

The effect of the size of the uncertainty region was investigated first. The uncertainty region refers to the symmetric interval box of *a priori* defined values around the nominal parameter values in which the uncertain parameters are bounded in a multi-scenario formulation (i.e. $\boldsymbol{\theta} \in [(1-\alpha)\boldsymbol{\theta^{nom}}, (1+\alpha)\boldsymbol{\theta^{nom}}]$), where the parameter α is used to represent the size of the uncertainty region. Given increasing sizes of uncertainty regions α, the robust controller

performance is expected to degrade since the uncertain parameters are able to take on a wider range of values, which the controller must accommodate for. The source of the performance degradation is of interest as it could manifest as less aggressive control action or set-point offset.

As mentioned above, a nominal NMPC was designed with the uncertain parameter values set to their corresponding nominal parameters (Table 5), which were the same values used in the plant for this scenario. This corresponds to the operational case where the model describes the plant perfectly, which may rarely occur in practice. As can be seen in Table 6, the nominal NMPC has no set-point offset in the %CC controlled variable. As mentioned above, the performance of the nominal NMPC was used to determine the PoR in order to compare multiple three-realization multi-scenario NMPCs that were also tested in the plant simulation. The three-realization multi-scenario NMPCs tested had increasingly large uncertainty region sizes (i.e. increasing α value). The scenarios in the three-realization controllers were defined at the nominal ($\boldsymbol{\theta^{nom}}$), minimal ($\boldsymbol{\theta^{l}} = (1-\alpha)\boldsymbol{\theta^{nom}}$), and maximal ($\boldsymbol{\theta^{h}} = (1+\alpha)\boldsymbol{\theta^{nom}}$) values of each uncertain parameter for the given size of uncertainty region. These controllers were tested in a disturbance rejection scenario, where two subsequent 5% steps down in total flowrate of flue gas (F_{in}^{g}) were implemented 44 time intervals (550 s) apart, as displayed in Figure 3. The 44 intervals between the steps were used to ensure sufficient time for the $\%CC$ output to reach steady state prior to disturbing the system again. Subsequent smaller steps down were implemented in favor of a single large step for ease of convergence in the IPOPT solver.

Table 6: Price of robustness, offset, and CPU time for increasing uncertainty region sizes

$\boldsymbol{\alpha}$	PoR (%)	Offset (%)	CPU time (s)
0 (nominal)	0	0	55.71
0.2	5.74	0.0253	183.14
0.25	9.57	0.0396	192.42
0.3	14.82	0.0568	192.74
0.35	21.77	0.0768	218.73
0.4	29.36	0.0968	208.27

Table 6 summarizes the results of these tests. As shown in this table, there is substantial performance degradation as reflected in the increasing PoR for increasing uncertainty region sizes. This degradation comes mostly in the form of offset as displayed in Figure 5. While the nominal NMPC shows no offset, each subsequent robust NMPC controller shows an increasing amount of offset with an increased uncertainty region size. A single-scenario NMPC with poorly chosen uncertain parameters (i.e. different than the nominal plant parameters), however, would not exhibit off-set free performance like the one exhibited by the nominal NMPC. This would be analogous to the case where a NMPC no longer has a perfect plant model (plant-model mismatch) and is where multi-scenario approach can be beneficial; this type of behavior is investigated in the following sections. It can be also observed in Figure 4 and Figure 5 that the conservatism is not reflected in the aggressiveness (or lack thereof) of the control actions as each plant reaches its new steady state at approximately similar times for all the robust NMPC controllers. These figures also show that small changes in the manipulated variable reflect with quite substantial changes in the controlled variable. The results in Table 6 also suggests that there is an increasing price of robustness difference for constant increases in size of the uncertainty region. This nonlinear relationship highlights the need to define an uncertainty region size that covers the expected uncertainty but not so large as to squander the potential benefit of the multi-scenario approach. Moreover, a

small increase in mean CPU time per simulation can generally be observed for increased sizes of uncertainty region. A similar effect was observed in a scheduling context by Li and Ierapetritou [58] and is explained by a decrease in the size of the feasible region making it more difficult to find a solution as robustness requirements increase.

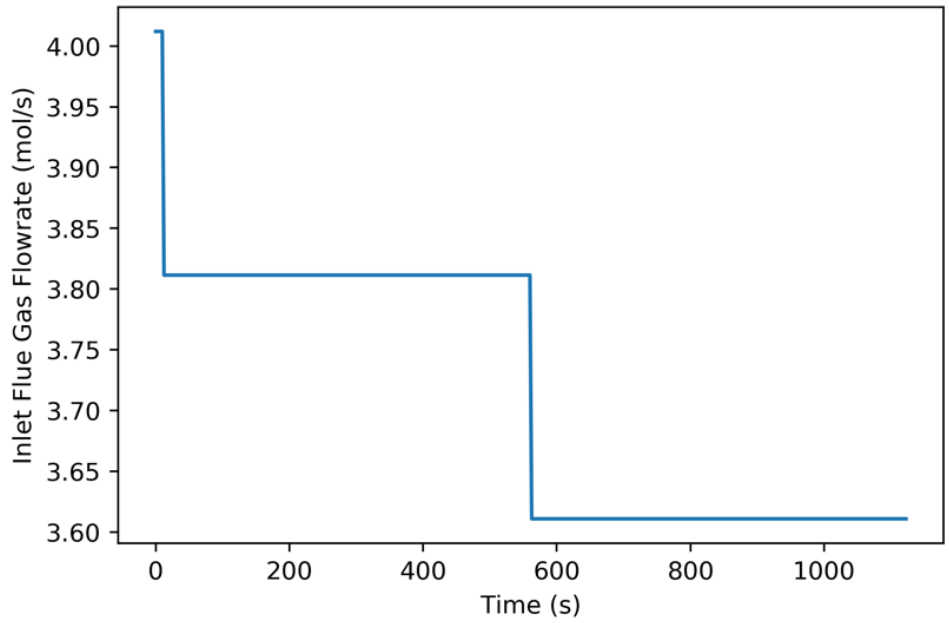

Figure 3: Inlet flue gas flowrate (disturbance) for Scenario A (5.1) and Scenario B (5.2)

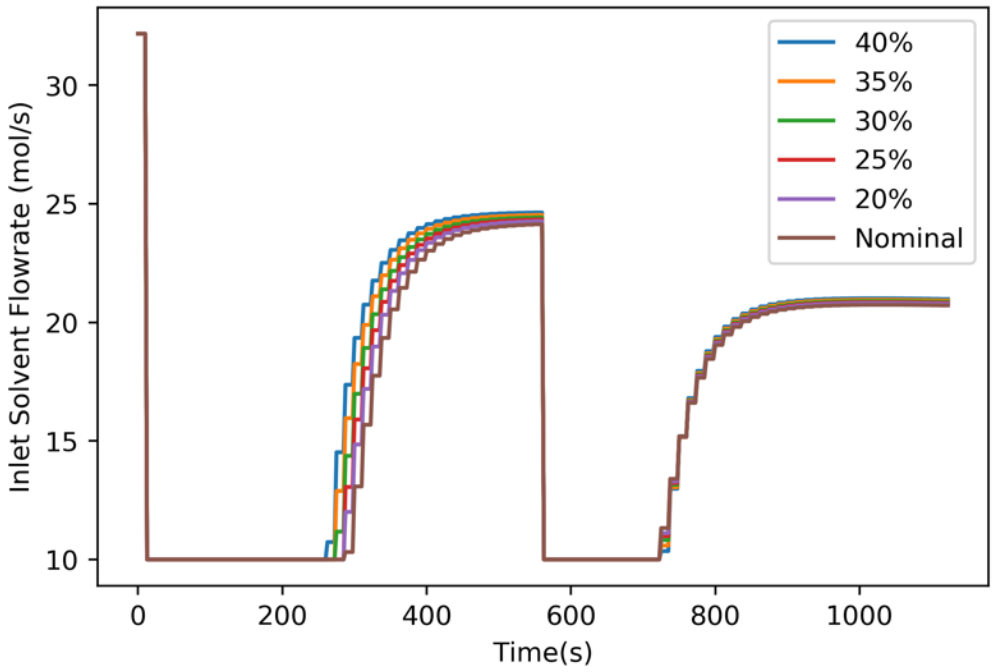

Figure 4: Inlet solvent flowrate (manipulated variable) for step-down simulations and increasing uncertainty region size

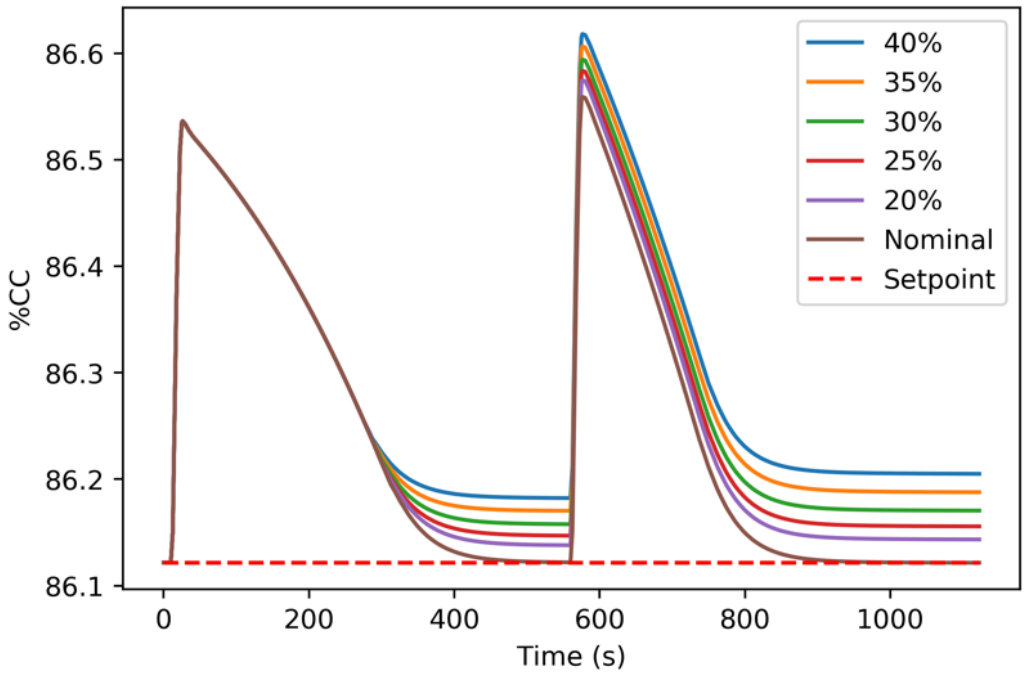

Figure 5: Percent Carbon capture (controller variable) for step-down simulations and increasing uncertainty region size

5.2. Scenario B: Effect of number of realizations

With the effect of uncertainty region size established, the effects of the number of scenarios considered by the controller on performance and CPU time were assessed. The size of the uncertainty region may be different for each parameter. In principle, historical plant data, seasonal and diurnal changes in the process, and process heuristics can be used to determine the size of the uncertainty. However, for the remainder of this work $\alpha = 0.3$ was chosen as the uncertainty region size for all of the uncertain parameters. This uncertainty region size was selected based on a preliminary analysis that showed that a 30% variation in the uncertain parameters represented significant process variability that is often observed during operation. Moreover, from the results of Scenario A, it was concluded that this uncertainty region size represents an acceptable trade-off between uncertainty region size (robustness) and PoR. Each of the uncertain parameters was discretized to its nominal, low or high values to limit the number of possible uncertainty realizations. Even with this limitation, since there exist four uncertain parameters that can occur at either θ^{nom}, θ^{l}, or θ^{h}; there are $3^4 = 81$ possible combinations of these parameters. However, including 81 realizations in a controller is unrealistic as the CPU time would become computationally intractable; thus, the maximum number of realizations allowed for a multi-scenario controller was chosen to be 7 based on observed CPU times and preliminary closed-loop simulations. These realizations are displayed in Table 7.

Table 7: Possible parameter realizations for the controllers and the plants

	S1 (P1)	**S2 (P2)**	**S3**	**S4 (P3)**	**S5**	**S6 (P4)**	**S7**
γ_{MEA}	θ^{nom}	θ^{h}	θ^{l}	θ^{h}	θ^{l}	θ^{l}	θ^{nom}
γ_{CO_2}	θ^{nom}	θ^{h}	θ^{l}	θ^{l}	θ^{l}	θ^{h}	θ^{nom}
γ_{H_2O}	θ^{nom}	θ^{h}	θ^{l}	θ^{h}	θ^{h}	θ^{nom}	θ^{nom}
$y_{in}^{CO_2}$	θ^{nom}	θ^{h}	θ^{l}	θ^{h}	θ^{h}	θ^{nom}	θ^{l}

These realizations were chosen with the goal of exploring a mix between expected and worst-case combinations of uncertain parameters. That is, the scenarios aim to represent (with only a few realizations), the full set of parameter realizations that may actually occur. It would be desirable to include a large number of these scenarios to make the controller robust; however, this number is limited by the CPU time. Note that the choice of these parameter realizations (as well as the number of realizations) in the controller can drastically affect closed-loop performance. Accordingly, the choice of realizations should be tailored to the specific application, especially when the operator has insight on the potential uncertainty. In this case specifically, each scenario was chosen as it represented a distinct combination of the uncertainty parameters that is significantly different from the other realizations in the uncertain parameter realization set.

While testing the performance of the multi-scenario controllers against a large sample of plants with different parameter realizations would be the best way to assess their benefit, time limitations required only simulating the controllers in a few plants, which itself still required significant computational effort. As such, a sample of four plants with different uncertain parameter realizations was chosen such that it would be as representative as possible to the potential variations in uncertain parameters and such that statistical measures approximately reflected the benefits of the multi-scenario controller. The chosen simulated plants contained the parameter value realizations in Table 7 that correspond to S1, S2, S4, and S6, i.e. P1, P2, P3 and P4, respectively. With regards to the parameter values displayed in Table 7, S1 was chosen as it contained only nominal parameter values, S2 was chosen as all values were at the same (high) uncertain region boundaries, S4 was chosen as it contained values that were at different (high and low) uncertainty region boundaries, and S6 was chosen as it contained a mixture of nominal and uncertainty region boundary uncertain parameters.

Robust NMPC controllers with three, five, and seven scenarios were evaluated on the aforementioned plants. Also, an NMPC with uncertain parameters values different that the nominal uncertain parameters was considered. The performance of the robust controllers was tested using the same disturbance rejection tests as in Scenario A, shown in Figure 3, with a shorter simulation time of 950 seconds. The shorter simulation time was introduced in order to cut down on the computational effort required to obtain the results. Nevertheless, it proved to be more than sufficient time for the systems to reach their new-steady state after both disturbances are introduced as shown in the results from Scenario A. In this scenario, however, the controllers were compared based on their performance indices, as displayed in Table 8.

*Table 8: Performance indices of various NMPCs and multi-scenario NMPCs in different plants (i.e. with different uncertain parameter realizations). The average column represents the average performance index of a given controller in all plants simulated ($\bar{J}_c$), with their respective standard deviations (σ_{J_c}). *Plants where controllers exhibited ringing for the default tuning parameters*

Controller	**Scenario(s)**	**J_c (P1)**	**J_c (P2)**	**J_c (P3)**	**J_c (P4)**	**Average $\bar{J}_c$**	**Std. Dev σ_{J_c}**	**Mean CPU (s)**	**No. of Equations**
C1 (Nominal)	S1	13.044	19.250	14.576	11.940	14.703	3.218	50.9	64,488
C2	S2	32.020	11.126	31.646	20.581	23.843	10.00	57.7	64,488
C3	S1, S2, S3	14.977	15.455	16.475	11.163	14.518	2.322	192.3	193,416
C4	S1, S2, S3, S4, S5	14.679	17.657	15.469	11.969	14.944	2.349	385.7	322,344

C5	S1, S2, S3, S4, S5, S6, S7	15.161	15.700	16.537	11.350	14.687	2.295	718.6	451,272

The results in Table 8 show that the mean CPU time increases as the robust controllers takes more realizations into account. This is expected as the size of the problem grows proportionally to the number of scenarios as reflected in the number of equations, thus increasing the size of the search space that the NLP solver must consider. The degrees of freedom for each problem, however, remained fixed at eight (time intervals in the control horizon) regardless of the number of realizations considered in the controller. Nevertheless, since the total model size does grow with realizations, it is crucially important to determine whether the sacrifice in computational effort in the multi-scenario controllers is worth the increased robustness. For instance, consider C2 (an NMPC controller with parameters on the high end of uncertainty region) and C5 (the seven-scenario controller). The mean performance index across all plants tested is ~1.62 times higher for C2 while the mean CPU time is time is ~12.45 times higher for C5. On face value, it appears that for the additional computational effort required for C5 to be justified, the operator must be placing significant priority to performance. However, this experiment only simulates approximately 16 minutes of plant operation. This is a relatively short amount of time where only two step-changes in the upstream process are introduced into the plant. A longer simulation time, which is unrealistic to perform for all controllers in all plants due to time constraints, would better illustrate the performance disparity between the two controllers. Nevertheless, in a real test scenario the PCC absorber could be operating continuously for days provided that the downstream combustion process is operating.

Despite the large computational cost of C5, very similar performance improvement over C2 was achieved with the three-scenario controller (C3) without as much additional computational burden. The mean performance of C2 is ~1.64 times higher than that of C3, while the mean computational time of C3 is a much more reasonable (compared to C5) ~3.33 times higher than that of C2. This, with C3 the operator would still be placing priority on performance over computational burden but not nearly as much as with C5. As mentioned above, this performance disparity would become increasingly large with longer test times as more error accrues in the performance indices. Although the performance of C3 and C5 are very similar despite much larger mean CPU times for C5, it should be noted that this is likely due to the small sample of plants used in this study. Across a larger set of plants, we would expect to see a clear benefit when using C5 since it is the most robust controller.

As indicated in Section 5, the uncertain parameters have been chosen to be uniformly distributed with their nominal parameter values in the center of the distribution. As a result, C1, which contains the uncertain parameters' nominal values that are centrally positioned in the uncertainty region; is expected to have some inherent robustness and therefore present good performance in most plant cases (as show in Table 8). This is analogous to the case where a NMPC is designed with well-chosen/estimated parameters and is reflected in C1s average performance index ($\overline{J_c}$ in Table 8), which is closer to that of the robust multi-scenario controllers (C3,C4, and C5) than that of the other single-scenario controller with large plant-model mismatch (i.e. C2). However, it is not always the case that parameters can be well chosen/estimated, i.e. when the parameter estimation problem is too large, not repeated frequently enough, or when variables are approximated as parameters. To contrast, C2 (i.e. the NMPC with parameter values at the high end of the uncertainty region) was observed to show substantially worse performance than C1, as reflected in the average

performance index of C1 which is ~0.617 times that of C2. This is because C2 lacks the inherent robustness imparted on C1 by having centrally located parameter values in the uncertainty region and is analogous to the case where the NMPC is designed with poorly chosen/estimated parameters. Moreover, for C1 and C2, we observe a larger standard deviation in their performance across plants. This is particularly evident in C2 but still noticeable with C1. This means that these controllers show more variation in their performance in different plants (i.e. good performance in some plants and poor performance in others). Take for instance C1, which performs well relative to other controllers in P1 but less so in P2. C1s performance in P1 should be very good as its single scenario contains no plant-model mismatch to P1. However, its performance in P2 is worse because all the parameter values are largely mismatched; the converse can be said about C2. In contrast, the multi-scenario controllers show a more consistent performance among the different plants tested as reflected in their low deviations for the plant sample although the mean performances indices are very similar to that of C1. Having consistent operation despite uncertainty, such as the proposed robust NMPC enables, is crucial for a process like PCC as its economics and emissions must be controllable to be attractive for industrial implementation. Load changes in the upstream power plant are common and cause these operational disturbances, making it important to consider them on a model level.

Since we are assessing the controllers based on their performance index, it is important to notice that the experiment designed in this section has two subsequent transients and little time for the $\%CC$(controlled variable) to be at steady-state. More time at steady-state and longer simulations times would allow the performance index to accrue more error and the benefits of the robust controllers would be even more pronounced as they would display reduced set point offset. This effect will be shown in the next section as we consider a prolonged test case that the controller might encounter in a real MEA-based PCC absorber's daily operation.

5.3. Scenario C: Diurnal variation in flue gas

As stated above, the absorber's operation will occur downstream from a CO_2 emission source resulting in exogenous disturbances to the PCC plant operation. Coal-fired power plants are of specific interest to be retrofitted with PCC units and, as such, the coal-fired power plant will dictate the daily operational variation of the PCC plant. Conveniently, this provides a realistic test case under which the robust NMPC designed for the MEA PCC absorber can be evaluated for a longer operational period than in Section 5.2.

Due to diurnal variation in consumer demands, energy consumption occurs in a cyclical manner whereby the demand is highest in the middle of the day and lowest during the night. Similarly, for a region that is dependent on coal-fired power, the demand to the plant will also be cyclical leading to a periodic variation in the quantity of flue gas released. This periodic variation in the flue gas released by the plant provides a periodic disturbance to the MEA PCC plant. An example of region that is reliant on coal-fire power and experiences a diurnal demand variation is the Canadian province of Alberta. Based on an single-day data from the Alberta Electric System Operator (AESO), the cycle amplitude of the province's daily internal load is ~8.95% of the midline (average load) [59].

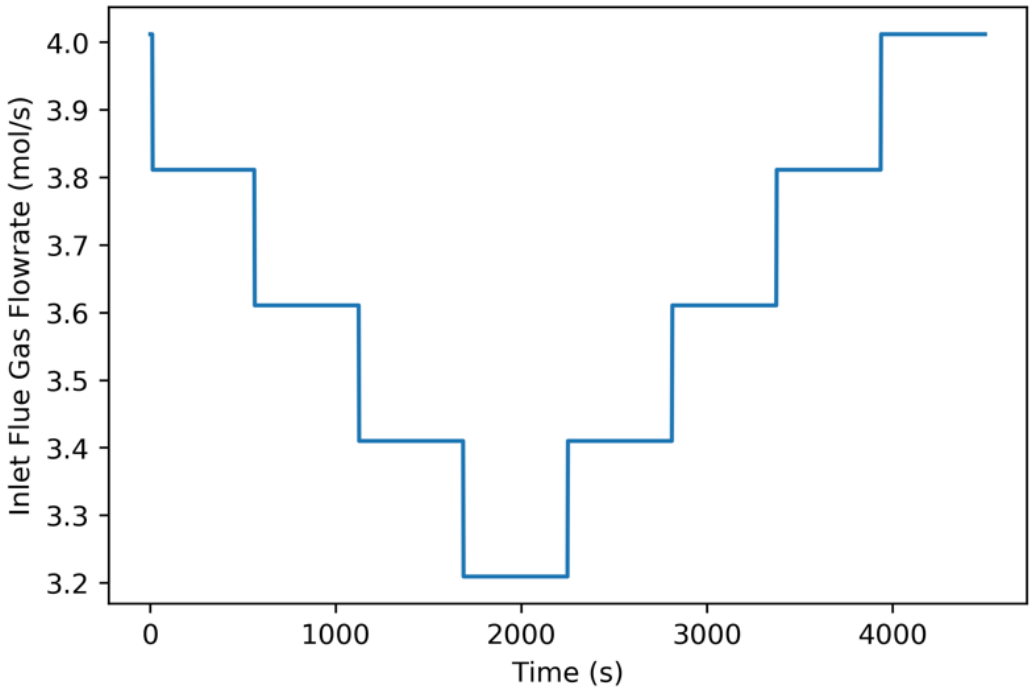

Figure 6: Diurnal Inlet flue gas flowrate variation (disturbance) for Scenario C (5.3)

As such, the disturbance in the flue gas flowrate shown in Figure 6 was used to approximate the single-day cycle in order to test the efficacy of several controllers for a single cycle. The periodic behavior was approximated as step changes in the flue gas flowrate to the absorber every 45 sampling intervals (~9.4 minutes). The amplitude of the variation in flue gas flowrate was assumed to be 10% of the midline flowrate based on the aforementioned daily observations from AESO. The cycle length was compressed to 75 minutes due to time limitations as a 24h simulation would be prohibitively long. Nonetheless, all controllers were shown to exhibit fast enough responses to reject each step disturbance before a subsequent one was introduced into the system.

For this test case, NMPC controllers involving one and three-scenarios ($\alpha = 0.3$) were implemented. The three-scenario robust NMPC controller was chosen as it could be shown to have benefits over single-scenario NMPCs with plant model-mismatch as demonstrated in section 5.2 while maintaining more acceptable computational costs relative to higher-scenario controllers. Specifically, controllers C1, C2, and C3 (Table 8) were implemented in P1, i.e. plant with nominal uncertain parameters (Table 7). Moreover, to further elucidate the benefits of the multi-scenario controller more clearly, uncertain parameters values for a second test plant were randomly generated (based on a uniform distribution) inside the 30% uncertainty region. In addition to testing C1, C2, and C3 for a longer simulation in P1, the controllers were also implemented in this plant (P5) using random values in the uncertain parameters. The parameter values for P5 are displayed in Table 9.

Table 9: Randomly determined uncertain parameter realization for Plant 5

Uncertain Parameter (θ)	$\boldsymbol{\theta_{P5}}$
γ_{MEA}	0.846
γ_{CO_2}	0.453
γ_{H_2O}	1.062

$y_{in}^{CO_2}$	0.182

Table 10: Performance indices and CPU times for single-scenario (C1 & C2) and multi-scenario (C3) NMPCs in Plant 1 and Plant 5

Controller	***Scenario(s)***	J_c ***(P1)***	***Mean CPU (s)***	J_c ***(P5)***	***Mean CPU (s)***
C1 (Nominal)	S1	33.143	74.135	66.281	47.427
C2	S2	157.647	79.583	71.593	58.422
C3	S1, S2, S3	39.021	186.750	35.151	202.908

Table 10 summarizes the results for this scenario. As expected, the multi-scenario controller (C3) exhibited far better performance than the single-scenario NMPC with plant-model mismatch (i.e. C2) in P1. This was markedly illustrated by the longer simulation length of 75 minutes in this scenario compared to 18.75 minutes in the simulation from Scenario B. This is further exhibited in Figure 7,where the performance of C3 when employed in P1 is much more like the performance of the C1 (nominal controller) than that of C2 (controller with plant-model mismatch). Moreover, although the robust controller (C3) requires on average ~2.35 times the computational effort of C2, its performance index is ~0.25 times that of C2, thus justifying the additional computational effort. This reinforces the notion that the robust controller's benefits are more clearly observed over a longer operating window.

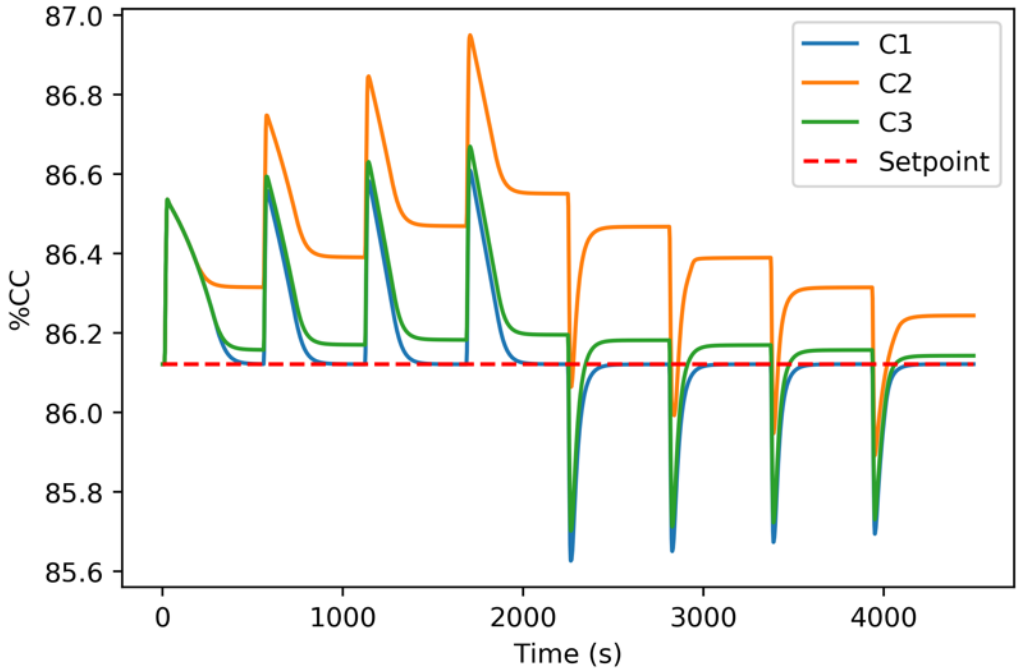

Figure 7: Percent Carbon capture for diurnal variation in flue gas simulations in P1

In P5 (random plant uncertain parameter realization), both C1 and C2 performed relatively similarly with respect to performance indices and CPU times as shown in

Table 10. However, as with P1, the robust NMPC controller (C3) exhibited a better performance index that is half of that observed for C1 and C2. Note that in this case, C1 (nominal NMPC) has plant-model mismatch because plant P5 contains random realizations in the uncertain parameters, which no longer correspond to those in C1. This robustness came at a significant computational cost as each NMPC execution for C3 required ~4 times the CPU time relative to C1 and C2. Nevertheless, as shown in the simulations over a longer operational time, the benefits of a robust NMPC are evident even when only a small number of scenarios are considered. This performance benefit accrues over time and is significant in a plant that operates continuously for several hours or days such as a PCC plant. The simulations performed in this section, although longer than that shown in the previous scenario, are still relatively short compared to the operational time of a PCC plant. Consequently, real plant operation would see even more pronounced benefits from using the multi-scenario approach. As mentioned earlier, consistent performance despite uncertainty is essential to the PCC process. We have demonstrated in this scenario that, given a realistic load following experiment, the robust controller has superior regulatory performance for the %CC set-points. Having robust control, such as that presented in this work, makes the process industrially viable given the importance of economics and emissions.

6. Conclusions and future work

A robust NMPC for a post-combustion CO_2 capture absorber was presented. The robust operation of the absorber under parametric and process uncertainty using the robust NMPC controller was compared against that of nominal and plant-model mismatched NMPCs for various disturbance rejection scenarios. This is the first explicit treatment of uncertainty associated with operating conditions and physical property descriptions in the MEA PCC process and it was enabled by the use of a dynamic mechanistic model. The controllers were assessed in a simulated plant with plant-model mismatch to elucidate the benefits of the multi-scenario approach used in the design of the robust NMPC. As expected, the computational demands of the robust NMPC controllers were found to be increasing with increasing size of uncertainty regions and increasing number scenarios considered by the controller. Moreover, a larger uncertainty region was found to exhibit more conservativism in the control moves leading to offset. Nevertheless, it was found that for short simulation times the robust NMPCs generally led to better average performance and less variability in performance across plants in which the controllers were tested. Further, for long simulations, where error can accrue over time; the performance of a robust NMPC controller was found to be significantly better than that of the NMPCs with no robustness.

There remain a few issues to be solved before an approach using this nonlinear model becomes tractable. Namely, a reduction in CPU time is necessary for online implementation of the NMPCs presented in this study. This computational effort reduction can be achieved with fast NMPC algorithms, which use model reduction [60] and advanced step strategies [61]. However, model reduction strategies may not be able to capture process nonlinearities and may not be able to consider parametric uncertainty in the same level of detail as presented in this study. Thus, advanced dynamic optimization decomposition techniques may be considered to reduce the computational effort. Furthermore, this work operates under the assumption of full access to the plant states. Accordingly, a state estimation method for this system is also required and is a problem that has not been addressed in the literature for the CO_2 absorber system. To this end, conventional estimation methods such as Kalman filter (KF) and extended Kalman filter (EKF), or optimization methods like moving horizon estimation (MHE) can be considered. Likewise, as shown in this

work, the robust NMPC controllers do not have perfect performance and result in some set-point offset. A natural extension of the multi-scenario-based robust controller to further reduce this conservatism is the design of a multi-stage robust controller [62]. Furthermore, the scope of this work was limited to the application of the robust NMPC controller to the absorber in the PCC plant, a natural extension to this would be its application to the full PCC plant. This will come with additional computational challenges as considering the complete plant in a mechanistic model would result in an even larger optimization problem than that presented in this study.

Acknowledgements

The authors would like to acknowledge the Natural Sciences and Engineering Research Council of Canada (NSERC) for their financial support.

References

[1] J. Olivier and J. Peters, Trends in Global CO2 and Total Greenhouse Gas Emissions: 2018 Report. PBL Netherlands Environmental Assessment Agency. The Hague, 2018.

[2] BP p.l.c. BP Statistical Review of World Energy 2019. London, 2019.

[3] Le Quéré, C., Andrew, R. M., Friedlingstein, P., Sitch, S., Hauck, J., Pongratz, J., Pickers, P. A., Korsbakken, J. I., Peters, G. P., Canadell, J. G., Arneth, A., Arora, V. K., Barbero, L., Bastos, A., Bopp, L., Chevallier, F., Chini, L. P., Ciais, P., Doney, S. C., Gkritzalis, T., Goll, D. S., Harris, I., Haverd, V., Hoffman, F. M., Hoppema, M., Houghton, R. A., Hurtt, G., Ilyina, T., Jain, A. K., Johannessen, T., Jones, C. D., Kato, E., Keeling, R. F., Goldewijk, K. K., Landschützer, P., Lefèvre, N., Lienert, S., Liu, Z., Lombardozzi, D., Metzl, N., Munro, D. R., Nabel, J. E. M. S., Nakaoka, S.-I., Neill, C., Olsen, A., Ono, T., Patra, P., Peregon, A., Peters, W., Peylin, P., Pfeil, B., Pierrot, D., Poulter, B., Rehder, G., Resplandy, L., Robertson, E., Rocher, M., Rödenbeck, C., Schuster, U., Schwinger, J., Séférian, R., Skjelvan, I., Steinhoff, T., Sutton, A., Tans, P. P., Tian, H., Tilbrook, B., Tubiello, F. N., van der Laan-Luijkx, I. T., van der Werf, G. R., Viovy, N., Walker, A. P., Wiltshire, A. J., Wright, R., Zaehle, S., and Zheng, B. Global Carbon Budget 2018. Earth Syst. Sci. Data, 10, 2141-2194, 2018. https://doi.org/10.5194/essd-10-2141-2018

[4] P. Linga, R. Kumar and P. Englezos. The clathrate hydrate process for post and pre-combustion capture of carbon dioxide. Journal of Hazardous Materials, vol. 149, no. 3, pp. 625-629, 2007. https://doi.org/10.1016/j.jhazmat.2007.06.086

[5] P. Babu, R. Kumar and P. Linga. Pre-combustion capture of carbon dioxide in a fixed bed reactor using the clathrate hydrate process. Energy, vol. 50, pp. 364-373, 2013. https://doi.org/10.1016/j.energy.2012.10.046.

[6] D. Valencia-Marquez, A. Flores-Tlacuahuac and L. Ricardez-Sandoval. Technoeconomic and Dynamical Analysis of a CO2 Capture Pilot-Scale Plant Using Ionic Liquids. Industrial & Engineering Chemistry Research, vol. 54, no. 45, pp. 11360-11370, 2015. https://doi.org/10.1021/acs.iecr.5b02544.

[7] Lucio, M. and Ricardez-Sandoval, L. Dynamic modelling and optimal control strategies for chemical-looping combustion in an industrial-scale packed bed reactor. Fuel, 262, p.116544, 2019. https://doi.org/10.1016/j.fuel.2019.116544.

[8] H. You, Y. Yuan, J. Li and L. Sandoval. A Multi-scale model for CO2 capture: A Nickel-based oxygen carrier in Chemical-looping Combustion. IFAC-PapersOnLine, vol. 51, no. 18, pp. 97-102, 2018. https://doi.org/10.1016/j.ifacol.2018.09.264.

[9] A. Chansomwong, P. Douglas, E. Croiset, K. Zanganeh, A. Shafeen and L. Ricardez-Sandoval. Control of An Oxy-fuel Capture and Purification Unit For Coal-Based Power Plants. Energy Procedia, vol. 63, pp. 476-483, 2014. https://doi.org/10.1016/j.egypro.2014.11.051.

[10] A. Chansomwong, K. Zanganeh, A. Shafeen, P. Douglas, E. Croiset and L. Ricardez-Sandoval. Dynamic modelling of a CO2 capture and purification unit for an oxy-coal-fired power plant. International Journal of Greenhouse Gas Control, vol. 22, pp. 111-122, 2014. https://doi.org/10.1016/j.ijggc.2013.12.025.

[11] M. Wang, A. Lawal, P. Stephenson, J. Sidders and C. Ramshaw. Post-combustion CO2 capture with chemical absorption: A state-of-the-art review. Chemical Engineering Research and Design, vol. 89, no. 9, pp. 1609-1624, 2011. https://doi.org/10.1016/j.cherd.2010.11.005.

[12] E. Dugas. Pilot plant study of carbon dioxide capture by aqueous monoethanolamine. Masters thesis, University of Texas at Austin, 2006.

[13] R. Idem et al. Pilot Plant Studies of the CO2Capture Performance of Aqueous MEA and Mixed MEA/MDEA Solvents at the University of Regina CO2Capture Technology Development Plant and the Boundary Dam CO2Capture Demonstration Plant. Industrial & Engineering Chemistry Research, vol. 45, no. 8, pp. 2414-2420, 2006. https://doi.org/10.1021/ie050569e.

[14] B. Huang et al. Industrial test and techno-economic analysis of CO2 capture in Huaneng Beijing coal-fired power station. Applied Energy, vol. 87, no. 11, pp. 3347-3354, 2010. https://doi.org/10.1016/j.apenergy.2010.03.007.

[15] L. Faramarzi et al. Results from MEA Testing at the CO2 Technology Centre Mongstad: Verification of Baseline Results in 2015. Energy Procedia, vol. 114, pp. 1128-1145, 2017. https://doi.org/10.1016/j.egypro.2017.03.1271.

[16] S. Bahakim and L. Ricardez-Sandoval. Optimal Steady-state Design of a Post-combustion CO2 Capture Plant Under Uncertainty. Energy Procedia, vol. 63, pp. 1608-1616, 2014. https://doi.org/10.1016/j.egypro.2014.11.171.

[17] S. Bahakim and L. Ricardez-Sandoval. Optimal Design of a Postcombustion CO2 Capture Pilot-Scale Plant under Process Uncertainty: A Ranking-Based Approach. Industrial & Engineering Chemistry Research, vol. 54, no. 15, pp. 3879-3892, 2015. https://doi.org/10.1021/ie5048253.

[18] J. Gaspar, L. Ricardez-Sandoval, J. Jorgensen and P. Fosbøl. Dynamic simulation and analysis of a pilot-scale CO2 post-combustion capture unit using piperazine and MEA. IFAC-PapersOnLine, vol. 49, no. 7, pp. 645-650, 2016. https://doi.org/10.1016/j.ifacol.2016.07.246.

[19] J. Gaspar, L. Sandoval, J. Jørgensen and P. Fosbøl. Design, Economics and Parameter Uncertainty in Dynamic Operation of Post-combustion CO2 Capture Using Piperazine (PZ) and MEA. Energy Procedia, vol. 114, pp. 1444-1452, 2017. https://doi.org/10.1016/j.egypro.2017.03.1269.

[20] A. Lawal, M. Wang, P. Stephenson and H. Yeung. Dynamic modelling of CO2 absorption for post combustion capture in coal-fired power plants. Fuel, vol. 88, no. 12, pp. 2455-2462, 2009. https://doi.org/10.1016/j.fuel.2008.11.009.

[21] N. Mac Dowell, N. Samsatli and N. Shah. Dynamic modelling and analysis of an amine-based post-combustion CO2 capture absorption column. International Journal of Greenhouse Gas Control, vol. 12, pp. 247-258, 2013. https://doi.org/10.1016/j.ijggc.2012.10.013.

[22] T. Nittaya, P. Douglas, E. Croiset and L. Ricardez-Sandoval. Dynamic Modeling and Evaluation of an Industrial-Scale CO2Capture Plant Using Monoethanolamine Absorption Processes. Industrial & Engineering Chemistry Research, vol. 53, no. 28, pp. 11411-11426, 2014. https://doi.org/10.1021/ie500190p.

[23] M. Hossein Sahraei and L. Ricardez-Sandoval, "Controllability and optimal scheduling of a CO 2 capture plant using model predictive control", International Journal of Greenhouse Gas Control, vol. 30, pp. 58-71, 2014. https://doi.org/10.1016/j.ijggc.2014.08.017.

[24] N. Haimour and O. Sandall, "Absorption of carbon dioxide into aqueous methyldiethanolamine", Chemical Engineering Science, vol. 39, no. 12, pp. 1791-1796, 1984. https://doi.org/10.1016/0009-2509(84)80115-3.

[25] H. Hikita, S. Asai, H. Ishikawa and M. Honda, "The kinetics of reactions of carbon dioxide with monoethanolamine, diethanolamine and triethanolamine by a rapid mixing method", The Chemical Engineering Journal, vol. 13, no. 1, pp. 7-12, 1977. https://doi.org/10.1016/0300-9467(77)80002-6.

[26] K. Hoff, O. Juliussen, O. Falk-Pedersen and H. Svendsen, "Modeling and Experimental Study of Carbon Dioxide Absorption in Aqueous Alkanolamine Solutions Using a Membrane Contactor", Industrial & Engineering Chemistry Research, vol. 43, no. 16, pp. 4908-4921, 2004. https://doi.org/10.1021/ie034325a.

[27] H. Kvamsdal, J. Jakobsen and K. Hoff, "Dynamic modeling and simulation of a CO2 absorber column for post-combustion CO2 capture", Chemical Engineering and Processing: Process Intensification, vol. 48, no. 1, pp. 135-144, 2009. https://doi.org/10.1016/j.cep.2008.03.002.

[28] K. ONDA, H. TAKEUCHI and Y. OKUMOTO, "MASS TRANSFER COEFFICIENTS BETWEEN GAS AND LIQUID PHASES IN PACKED COLUMNS", Journal of Chemical Engineering of Japan, vol. 1, no. 1, pp. 56-62, 1968. https://doi.org/10.1252/jcej.1.56.

[29] N. Harun, T. Nittaya, P. Douglas, E. Croiset and L. Ricardez-Sandoval, "Dynamic simulation of MEA absorption process for CO2 capture from power plants", International Journal of Greenhouse Gas Control, vol. 10, pp. 295-309, 2012. https://doi.org/10.1016/j.ijggc.2012.06.017.

[30] S. Jayarathna, B. Lie and M. Melaaen, "Amine based CO2 capture plant: Dynamic modeling and simulations", International Journal of Greenhouse Gas Control, vol. 14, pp. 282-290, 2013. https://doi.org/10.1016/j.ijggc.2013.01.028.

[31] R. Schneider, E. Kenig and A. Górak, "Dynamic Modelling of Reactive Absorption with the Maxwell-Stefan Approach", Chemical Engineering Research and Design, vol. 77, no. 7, pp. 633-638, 1999. https://doi.org/10.1205/026387699526683.

[32] M. Luu, N. Abdul Manaf and A. Abbas. Dynamic modelling and control strategies for flexible operation of amine-based post-combustion CO 2 capture systems. International Journal of Greenhouse Gas Control, vol. 39, pp. 377-389, 2015. https://doi.org/10.1016/j.ijggc.2015.05.007.

[33] E. Mechleri, A. Lawal, A. Ramos, J. Davison and N. Dowell. Process control strategies for flexible operation of post-combustion CO 2 capture plants. International Journal of Greenhouse Gas Control, vol. 57, pp. 14-25, 2017. https://doi.org/10.1016/j.ijggc.2016.12.017.

[34] Bedelbayev, A., Greer, T. and Lie, B. MODEL BASED CONTROL OF ABSORPTION TOWER FOR CO2 CAPTURING. 2008.

[35] M. Sahraei and L. Ricardez-Sandoval. Simultaneous Design and Control of the MEA Absorption Process of a CO2 Capture Plant. Energy Procedia, vol. 63, pp. 1601-1607, 2014. https://doi.org/10.1016/j.egypro.2014.11.170.

[36] Z. He, M. Sahraei and L. Ricardez-Sandoval. Flexible operation and simultaneous scheduling and control of a CO2 capture plant using model predictive control. International Journal of Greenhouse Gas Control, vol. 48, pp. 300-311, 2016. https://doi.org/10.1016/j.ijggc.2015.10.025.

[37] M. Panahi and S. Skogestad. Economically efficient operation of CO2 capturing process. Part II. Design of control layer. Chemical Engineering and Processing: Process Intensification, vol. 52, pp. 112-124, 2012. https://doi.org/10.1016/j.cep.2011.11.004.

[38] J. Åkesson et al. Nonlinear Model Predictive Control of a CO2 Post-Combustion Absorption Unit. Chemical Engineering & Technology, vol. 35, no. 3, pp. 445-454, 2012. https://doi.org/10.1002/ceat.201100480.

[39] B. Decardi-Nelson, S. Liu and J. Liu. Improving Flexibility and Energy Efficiency of Post-Combustion CO2 Capture Plants Using Economic Model Predictive Control. Processes, vol. 6, no. 9, p. 135, 2018. https://doi.org/10.3390/pr6090135.

[40] L. Teck Chan and J. Chen. Economic model predictive control of an absorber-stripper CO2 capture process for improving energy cost. IFAC-PapersOnLine, vol. 51, no. 18, pp. 109-114, 2018. https://doi.org/10.1016/j.ifacol.2018.09.284.

[41] K. Salvinder et al. An overview on control strategies for CO2 capture using absorption/stripping system. Chemical Engineering Research and Design, vol. 147, pp. 319-337, 2019. https://doi.org/10.1016/j.cherd.2019.04.034.

[42] A. Krasławski. Review of applications of various types of uncertainty in chemical engineering. Chemical Engineering and Processing: Process Intensification, vol. 26, no. 3, pp. 185-191, 1989. https://doi.org/10.1016/0255-2701(89)80016-9.

[43] Mesbah, A. Stochastic Model Predictive Control: An Overview and Perspectives for Future Research. IEEE Control Systems, vol. 36, no. 6, pp. 30-44, 2016. https://doi.org/10.1109/mcs.2016.2602087.

[44] Q. Zhang, R. Turton and D. Bhattacharyya. Nonlinear model predictive control and H robust control for a post-combustion CO2 capture process. International Journal of Greenhouse Gas Control, vol. 70, pp. 105-116, 2018. https://doi.org/10.1016/j.ijggc.2018.01.015.

[45] Huang, R., Patwardhan, S. and Biegler, L. Multi-Scenario-Based Robust Nonlinear Model Predictive Control with First Principle Models. Computer Aided Chemical Engineering, 27, pp.1293-1298, 2009. https://doi.org/10.1016/S1570-7946(09)70606-6

[46] X. Tian, R. Negenborn, P. van Overloop, J. María Maestre, A. Sadowska and N. van de Giesen. Efficient multi-scenario Model Predictive Control for water resources management with ensemble streamflow forecasts. Advances in Water Resources, vol. 109, pp. 58-68, 2017. https://doi.org/10.1016/j.advwatres.2017.08.015.

[47] P. Vaidya and E. Kenig. CO2-Alkanolamine Reaction Kinetics: A Review of Recent Studies. Chemical Engineering & Technology, vol. 30, no. 11, pp. 1467-1474, 2007. https://doi.org/10.1002/ceat.200700268.

[48] Geankoplis, C. Transport processes and separation process principles. 4th ed. Upper Saddle River, NJ: Prentice Hall, 2003.

[49] D. Austgen, G. Rochelle, X. Peng and C. Chen. Model of vapor-liquid equilibria for aqueous acid gas-alkanolamine systems using the electrolyte-NRTL equation. Industrial & Engineering Chemistry Research, vol. 28, no. 7, pp. 1060-1073, 1989. https://doi.org/10.1021/ie00091a028.

[50] H. Kvamsdal and G. Rochelle. Effects of the Temperature Bulge in CO2Absorption from Flue Gas by Aqueous Monoethanolamine. Industrial & Engineering Chemistry Research, vol. 47, no. 3, pp. 867-875, 2008. https://doi.org/10.1021/ie061651s.

[51] Poling, B., Prausnitz, J. and O'Connell, J. The properties of gases and liquids. New York: McGraw-Hill, 2007.

[52] Smith, J.M., Van Ness, H.C. and Abbott, M.M. Introduction to Chemical Engineering Thermodynamics. 7th International Edition, McGraw-Hill Chemical Engineering Series. McGraw-Hill, Boston, 2005.

[53] Hilliard, M. A Predictive Thermodynamic Model for an Aqueous Blend of Potassium Carbonate, Piperazine, and Monoethanolamine for Carbon Dioxide Capture from Flue Gas**.** PhD thesis, University of Texas at Austin, 2008.

[54] J. Ko, T. Tsai, C. Lin, H. Wang and M. Li. Diffusivity of Nitrous Oxide in Aqueous Alkanolamine Solutions. Journal of Chemical & Engineering Data, vol. 46, no. 1, pp. 160-165, 2001. https://doi.org/10.1021/je000138x.

[55] I. Cerrillo-Briones and L. Ricardez-Sandoval. Robust optimization of a post-combustion CO2 capture absorber column under process uncertainty. Chemical Engineering Research and Design, vol. 144, pp. 386-396, 2019. https://doi.org/10.1016/j.cherd.2019.02.020.

[56] Hart, W., Watson, J. and Woodruff, D. Pyomo: modeling and solving mathematical programs in Python. Mathematical Programming Computation, 3(3), pp.219-260, 2011. https://doi.org/10.1007/s12532-011-0026-8.

[57] Wächter, A. and Biegler, L. On the implementation of an interior-point filter line-search algorithm for large-scale nonlinear programming. *Mathematical Programming*, 106(1), pp.25-57, 2005. https://doi.org/10.1007/s10107-004-0559-y.

[58] Z. Li and M. Ierapetritou. Robust Optimization for Process Scheduling Under Uncertainty. Industrial & Engineering Chemistry Research, vol. 47, no. 12, pp. 4148-4157, 2008. https://doi.org/10.1021/ie071431u.

[59] Ets.aeso.ca. Alberta Electric System Operator: Current and Historical Market Reporting. [online] Available at: http://ets.aeso.ca/ [Accessed Aug 14. 2019].

[60] M. Yu, D. Miller and L. Biegler. Dynamic Reduced Order Models for Simulating Bubbling Fluidized Bed Adsorbers. Industrial & Engineering Chemistry Research, vol. 54, no. 27, pp. 6959-6974, 2015. https://doi.org/10.1021/acs.iecr.5b01270.

[61] V. Zavala and L. Biegler. The advanced-step NMPC controller: Optimality, stability and robustness. Automatica, vol. 45, no. 1, pp. 86-93, 2009. https://doi.org/10.1016/j.automatica.2008.06.011.

[62] S. Lucia and S. Engell. Multi-stage and Two-stage Robust Nonlinear Model Predictive Control. IFAC Proceedings Volumes, vol. 45, no. 17, pp. 181-186, 2012. https://doi.org/10.3182/20120823-5-nl-3013.00015.